Role of orbital selectivity on crystal structures and electronic states in $BiMnO_3$ and $LaMnO_3$ perovskites

Gheorghe Lucian Pascut[1,2] and Kristjan Haule[2]
[1]*MANSiD Research Center and Faculty of Forestry, Stefan Cel Mare University (USV), Suceava 720229, Romania*
[2]*Center for Materials Theory, Department of Physics & Astronomy, Rutgers University, Piscataway, New Jersey 08854, USA*

(Received 11 December 2021; revised 22 November 2022; accepted 10 January 2023; published 31 January 2023)

Correlated oxides, such as $BiMnO_3$ and $LaMnO_3$, show a complex interplay of electronic correlations and crystal structure exhibiting multiple first-order phase transitions, some without a clear order parameter. The quantitative theoretical description of this temperature-dependent electronic-structural interplay in the vicinity of a Mott transition is still a challenge. Here we address this issue by simultaneously considering both structural and electronic degrees of freedom, within a self-consistent density functional theory with embedded dynamical mean field theory. Our results show the existence of novel electronic states characterized by the coexistence of insulating, semimetallic, and metallic orbitals. This state is in agreement with resonant x-ray scattering. We also show that electronic entropy plays a decisive role in both electronic and structural phase transitions. By self-consistent determination of both the electronic state and the corresponding crystal structure, we show that the temperature evolution of these phases can be quantitatively explained from first principles, thus demonstrating the predictive power of the theoretical method for both the structural and the electronic properties.

DOI: 10.1103/PhysRevB.107.045147

I. INTRODUCTION

Manganese oxides with perovskite-type structure host a variety of interesting phenomena, among others the colossal magnetoresistance [1,2], insulator-to-metal transition [3], ferroelectricity coexisting with long-range magnetic order [4], and orbital and charge ordering [5]. The theoretical description of these functionalities is challenging, as the electronic correlations play an essential role, and the interplay between the electronic, orbital, and magnetic degrees of freedom with the crystal structure makes these materials extremely sensitive to small changes in external parameters, such as electric voltage, magnetic field, and temperature. However, this high sensitivity is a useful property, which is explored in the development of new electronic devices.

The theoretical methods for the *ab initio* description of strong correlations in solids have been recently developed, and among them the density functional theory with embedded dynamical mean field theory (DFT + eDMFT) [6–8] has demonstrated predictive power in many classes of correlated materials. For example, it was predicted that the magnetic moment in plutonium metal is screened at 800 K with valence fluctuations [9], which was subsequently verified by neutron scattering experiment [10]. An order of magnitude enhanced electron-phonon coupling in the FeSe superconductor as compared to the DFT result was predicted in Ref. [11], and subsequently verified by pioneering experiment using a combination of time-resolved photoemission spectroscopy coupled with x-ray diffraction [12]. Similarly, predictions of large fluctuating moments in iron superconductors and their energy distribution [13] have been later verified by neutron scattering [14]. The prediction of the isostructural metal-insulator transition under pressure in FeO has been confirmed in Ref. [15]. A novel type of long-ranged order with very high multipole ordering was proposed to explain the hidden order in URu_2Si_2 [16], which was confirmed by Raman scattering experiment [17]. Finally, structural relaxations by the eDMFT method have been recently developed [18], and it was demonstrated on the example of $NdNiO_3$ [19] and $Fe_2Mo_3O_8$ [20] that they can predict small changes of crystal structures near the Mott metal-insulator transition, the region which is challenging for other *ab initio* methods. In this paper we study the $AMnO_3$ class of materials with perovskite structure type to understand the role that correlations play in generating their rich phase diagrams [23–26]. We compare and contrast $LaMnO_3$ with $BiMnO_3$, which have attracted considerable interest due to the giant magnetoresistance phenomena in doped $LaMnO_3$ [1] and the potential multiferroic property in $BiMnO_3$ thin films [27,28].

The high-temperature (HT) phase ($T > 800$ K) of both $LaMnO_3$ and $BiMnO_3$ is a perovskite-type structure with orthorhombic symmetry [29–31] [see Fig. 1(a)] with similar bad-metallic conductivity [29,32–34]. At room temperature (RT) both compounds are insulating [29,35] and in $LaMnO_3$ the orthorhombic distortions increase with decreasing temperature but the symmetry remains orthorhombic [31], while in $BiMnO_3$ the structure distorts to monoclinic symmetry [36–38]. An abrupt change of resistivity is observed in both compounds around the transition, with the high-temperature phase exhibiting nearly temperature-independent resistivity, characteristic of a very bad metal. The pattern of structural distortions in both compounds is compatible with the long-range orbital ordering (OO) [31,36,39,40], which has been validated by resonant x-ray scattering (RXS) experiments

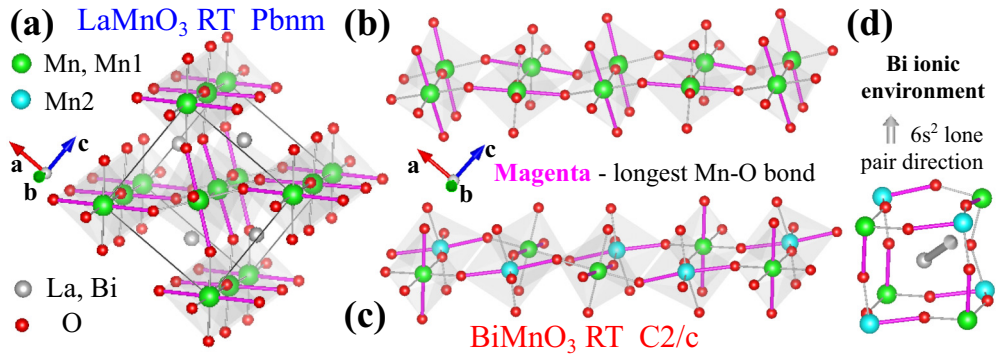

FIG. 1. Room temperature (RT) structural properties for $LaMnO_3$ and $BiMnO_3$. (a) Schematic view of the crystal structure for $LaMnO_3$. The longest Mn-O bond lengths are colored by magenta. (b) The octahedra distortion pattern in the (101) plane. (c) Distortions in $BiMnO_3$ in which Mn_1 ions show similar pattern to that in $LaMnO_3$, while in Mn_2 ions the long-bond distortions are confined to (101) plane. (d) Schematic view of Bi environment within a perovskite-like crystal structure; the gray arrow, pointing toward the face of the Mn_2O_6 octahedra, shows the direction of the $6s^2$ lone-pair electronic cloud within the Bi ionic environment [21]. The presence of the $6s^2$ lone pair is responsible for the appearance of two inequivalent Mn sites. Drawings were produced by VESTA [22].

[41–43] [see Figs. 1(b) and 1(c)]. The theoretical description of this Mott-type transition is most often described within the phenomenological models of the cooperative Jahn-Teller (JT) effect due to the Mn-d^4 configuration in octahedra, leaving a single electron in the e_g shell [21,24,32,44–47]. However, the two e_g orbitals are not degenerate in the high-temperature metallic phase, therefore the conventional JT mechanism does not apply, and better explanation of the transition is called for. Moreover, experimentally it was found that $BiMnO_3$ undergoes two phase transitions: A structural phase transition from orthorhombic to monoclinic symmetry takes place at $T = 768$ K [29], followed by another isostructural phase transition at $T = 474$ K [29,36,48]. While orbital order is symmetry-allowed at the first transition, RXS experiments showed that the situation is more complicated [43]. There is a sharp mean-field type upturn of the forbidden Bragg peak intensity at $T = 768$ K followed by the saturation regime. Below the second transition ($T = 474$ K), there is a second sharp upturn of the intensity, signaling that the long-range orbital order is well established only below the second phase transition ($T < 474$). The forbidden Bragg peak intensity in the intermediate phase (474 K $< T <$ 768 K) saturates to $\approx$0.6 of the room temperature intensity, which suggests that the intermediate phase has some type of partial order, but the nature of this partial order remains unknown. Both transitions are of first order, but the second isostructural transition does not have a clear order parameter.

The Mott transition and the Jahn-Teller distortion in $LaMnO_3$ have been previously studied by the dynamical mean field method using the minimal Hubbard model for the e_g electron, while the t_{2g} electrons were treated semiclassically, as a classical spin S with random orientation [49,50]. In this approach the effect of covalency is ignored, which was shown by x-ray absorption spectroscopy (XAS) to be important for interpretation of the XAS data [51]. Nevertheless, the metal-insulator transition was well captured by this minimal-model approach [49,50]. In Ref. [49] the transition temperature to the disordered state was somewhat underestimated, because the feedback effect of electronic correlations on crystal structure was ignored. This was partially corrected in Ref. [50] by allowing JT distortion, although the full structural relaxation was not attempted. Nevertheless a much better estimate for the transition temperature was reported, despite the fact that the electronic entropy was ignored in the calculation of energy. On the other hand, the complex phase diagram of $BiMnO_3$ has not been theoretically addressed before.

II. METHODS

To understand the unusual Mott transition coupled with the partial orbital order from first principles, we use the DFT + eDMFT method [6,8]. Here the downfolding to Hubbard-type models is avoided, and the dynamic correlations are added only to the very localized $3d$ orbitals, which is the solution of the Schrödinger equation inside a sphere centered on the Mn ion (radius 1.93 bohrs). The double counting between the DFT and DMFT correlations is treated within a nominal scheme, where the double counting is given by $U(n_f^0 - \frac{1}{2}) - \frac{J}{2}(n_f^0 - 1)$, with n_f^0 being the nominal occupancy of the d orbital [52]. The Coulomb repulsion on these quasiatomic orbitals used in this work has the Slater form in its fully rotational invariant form with its values estimated by constrained eDMFT to be $U = 10$ eV, $J = 1.18$ eV.

All crystal structures, except the high-temperature orthorhombic structure of $BiMnO_3$, were experimentally determined [30,31,36], and we checked that they agree very well with the theoretically determined optimized crystal structures (see Ref. [53]). We note that the force in our approach is calculated from the derivative of the free energy, rather than total energy [18]; therefore it contains important effects of electronic entropy at finite temperature, which we find to be essential to describe the orbitally disordered state in the orthorhombic structure, with finite but small orthorhombic distortions. We also note that the high-temperature orthorhombic $BiMnO_3$ crystal structure has not been determined before, and here is predicted for the first time (see Ref. [54]). It would be desirable to confirm it experimentally.

TABLE I. Occupancy of the Mn orbitals $(n_{e_{g1}}, n_{e_{g2}})$, where $|e_{g1}\rangle \approx |3z^2-1\rangle$ and $|e_{g2}\rangle \approx |x^2-y^2\rangle$. Note that $n_{t_{2g1}} \approx n_{t_{2g2}} \approx n_{t_{2g3}} \approx 1$. The realized electronic states are band-Mott insulator (BMI), orbital-selective Mott (OSM) state, and site-orbital-selective Mott (SOSM) state.

$LaMnO_3$	$T = 300$ K	$T = 573$ K	$T = 798$ K
Mn	(0.98, 0.45)	(0.97, 0.46)	(0.76, 0.66)
state	BMI	BMI	OSM
$BiMnO_3$	$T = 300$ K	$T = 550$ K	$T = 760$ K
Mn_1	(0.98, 0.44)	(0.93, 0.47)	(0.72, 0.69)
Mn_2	(0.98, 0.44)	(0.73, 0.69)	(0.72, 0.69)
state	BMI	SOSM	OSM

III. RESULT AND DISCUSSION

A schematic view of the room temperature (RT) crystal structure of $LaMnO_3$ and $BiMnO_3$ compounds is shown in Fig. 1. It consist of one and two inequivalent corner-sharing MnO_6 octahedra in $LaMnO_3$ and $BiMnO_3$, respectively. The two inequivalent octahedra, denoted by Mn_1O_6 and Mn_2O_6, appear due to the lone pair of electrons derived from the Bi-6*s* orbital [21], whose direction is shown schematically by the gray arrow in Fig. 1(d). Note that the lone pair consist of electronic charge, occupying the space between the center of Bi and the Mn_2 ion [21], which we mark by the gray arrow.

To describe the Mn-3*d* orbitals, we use the local coordinate system attached to each Mn ion, in which the hybridization of each orbital with environment is minimal. As expected for octahedral environment, there are three t_{2g} and two e_g orbitals pointing toward the faces and corners of the octahedra, respectively. As shown in Fig. 1(d), the lone pairs are pointing toward the octahedron face of Mn_2 ions; thus for this ion type the t_{2g} orbitals are expected to hybridize with the lone pair strongly, while the orbitals of Mn_1 ion type should not directly feel the presence of the lone pair in $BiMnO_3$.

While the formal valence of the Mn ion is Mn^{3+}, our calculations show that due to covalency there are approximately $n_d \approx 4.4$ electrons on each Mn ion ($Mn^{2.6+}$), of which almost exactly three electrons are in the t_{2g} shell, and therefore $n_{e_g} \approx 1.4$. This is in good agreement with valence determined from XAS in Ref. [51] ($n_d \approx 4.5$), but it is in stark contrast with the earlier DMFT works in which the number of e_g electrons has been fixed to one electron per Mn.

The degree of the orbital order is usually measured by occupancy ratio $n_{e_{g1}}/(n_{e_{g1}} + n_{e_{g2}}) \equiv (c_2)^2$, which was estimated by neutron scattering to be $c_2 \approx 0.81$ at room temperature [31]. Table I gives the temperature dependence of the occupancies, as found by the eDMFT method. We note that the maximal orbital ordering is for $n_{e_{g1}} \approx 1$, but due to covalency $n_{e_{g2}}$ does not vanish in this limit; hence c_2 always remains smaller than 1. In $LaMnO_3$ we get $c_2 = 0.826$, in good agreement with estimates from Ref. [31]. In $LaMnO_3$ the orbital polarization changes very little as long as the system has sizable charge gap, while orbital polarization becomes very small in the bad-metal phase above $T = 798$ K. Since the two e_g orbitals are not equivalent in the high-temperature structure, there remains a small difference in the occupancy as long as the system is in the orthorhombic phase. We note that in the earlier DMFT work [49] such agreement with experiment could not be achieved, and it was assigned to negligence of the electron-phonon coupling. In the minimal Hubbard model the insulating state must have integer occupancy; hence the constrained $n_{e_{g1}} + n_{e_{g2}} = 1$ leads to $c_2 \approx 1$ when polarization is large ($n_{e_{g1}} \approx 1$). Hence we now understand that the earlier disagreement with experiment was due to negligence of Mn covalency.

In $BiMnO_3$ there is an intermediate phase, in which electronic occupancies on the two Mn atoms are very different. Mn_1 keeps orbital polarization close to its room temperature value, while Mn_2 loses its polarization in this temperature range. As we will see later from structural optimization, such result is hard to guess from crystal structure alone, as the Mn_2 octahedra remain quite distorted in this intermediate phase.

If Fig. 2 we show temperature evolution of the density of states (DOS) for both t_{2g} and e_g orbitals. We also display structural information of the experimental structure. Each octahedron has three different types of Mn-O bond lengths, which are displayed as red horizontal bars. We label them as short (s; ∼1.9), medium (m; ∼2.0), and long (l; $\gtrsim$ 2.1). We also provide distortion parameters for octahedra [22], namely, the bond distortion index $\mathbf{D} = 1000 \sum_{i=1}^{6} |l_i - l_{\rm av}|/(6\, l_{\rm av})$ and the bond angle variance $\mathbf{S} = \sum_{i=1}^{8} (\phi_i - 90^\circ)^2/7$. Here l_i and ϕ_i are the bond distances and bond angles, respectively. $l_{\rm av}$ is the average bond length. Compared to Ref. [22], we use a formula for **D** with a multiplying factor of 1000. **D** and **S** are zero for an ideal octahedron.

At all temperatures and in both compounds t_{2g} electrons are in the Mott insulating state, and remain gapped even in the high-temperature metallic phase (see Figs. 2 and 3). This can be verified by looking at the t_{2g} self-energy, which has a pole inside the gap even when the e_g density of states shows metallic behavior (see Ref. [55]). This state is commonly called the *orbital-selective Mott state* [56–58], and was first introduced in Ref. [56] to explain the properties of $Ca_{2-x}Sr_xRuO_4$ in which spin-1/2 local moments coexist with metallic transport. Such a picture of *frozen high-spin* t_{2g} electrons in $LaMnO_3$ was postulated already in the very early works on the double-exchange model [59–61], and was also assumed in the previous DMFT calculations within the minimal two-orbital Hubbard model [49,50]. In the limit of weak correlations among e_g electrons, coexisting with the *high-spin core* t_{2g} states, the DMFT problem maps to the ferromagnetic Kondo model, which was shown in Ref. [62] to explain qualitatively the giant magnetoresistance in doped $LaMnO_3$. Nevertheless, to the best our knowledge, direct DMFT simulations with equal dynamic treatment of both t_{2g} and e_g orbitals was lacking; hence the theoretical photoemission spectra and position of the t_{2g} states was unknown. Moreover, as we will see in $BiMnO_3$ the approximation of t_{2g} electrons as *frozen high-spin core* is not really adequate.

Figure 2(a) shows that the room temperature gap is between e_g states, in which the occupied part is strongly admixed with oxygen states. The orbital with larger occupation (e_{g1}) points along the longest Mn-O bond, while the less occupied orbital (e_{g2}) points toward the shorter bonds. The gap between e_g's is not of Mott type; hence we call this state the *band-Mott insulator*. The peak-to peak splitting between these low-energy states is between 1.8–2 eV in the orbital

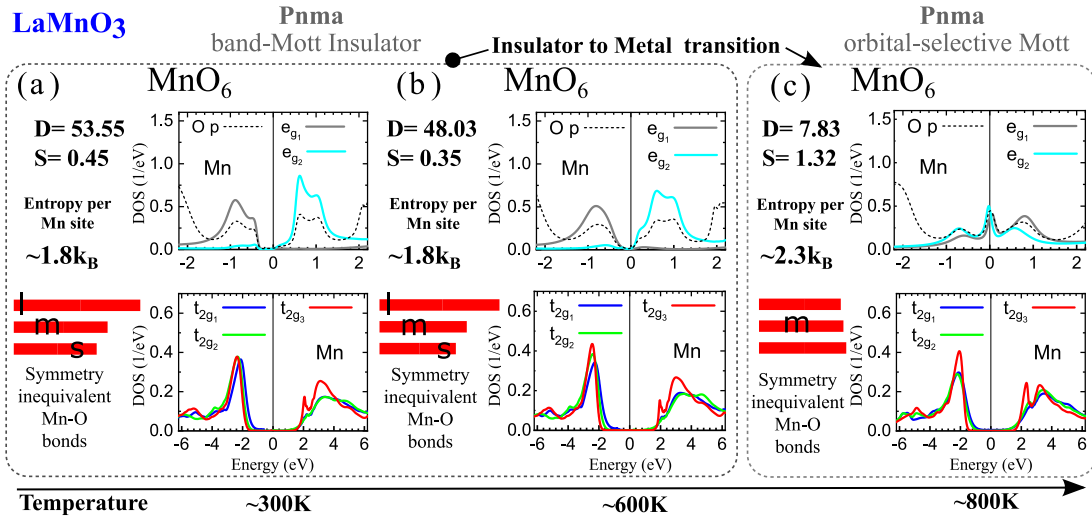

FIG. 2. Temperature-dependent electronic states in $LaMnO_3$. Panels (a) to (c) show for each inequivalent Mn octahedra the following properties: (1) values of the distortion indices, **D** and **S**; (2) electronic entropy per Mn site; (3) schematic view of the symmetry-inequivalent Mn-O bonds represented by red horizontal bars [the horizontal size of the bar is proportional to the bond length, short (s), medium (m), long (l); in panel (c) the three bonds are slightly distorted around the average bond length]; (4) e_g and t_{2g} projected density of states per formula unit versus energy in eV, for each electronic phase at a given temperature. On top of each panel we give the crystallographic symmetry at a given temperature and a name characterizing the electronic properties of the predicted electronic phases. The panels are connected by arrows suggesting the order parameter of the phase transitions.

ordered state, and the gap collapses around 800 K in the high-temperature orthorhombic structure, in which the three Mn-O bonds become very similar, although not strictly equal. Consequently, the two e_g orbitals are close to degenerate, but still different [see Fig. 2(c)]. The phase transition around 800 K is thus a first-order metal-insulator transition, strongly coupled with the structural evolution in which the distortion of the octahedra is strongly reduced, but the symmetry of the crystal structure does not change. This calculation shows not only that the details of the crystal structure and the lattice distortions have large impact on the electronic state, but also that the feedback effect of the electronic correlations on the crystal structure is crucial to properly describe the temperature evolution of the system. To understand whether structural distortions or electronic correlations drive the transition, we also calculate the electronic entropy [63] per Mn site at three temperatures as shown in Fig. 2. While normally the metallic phase has small entropy, and the Mott insulating state carries large entropy, here the situation is very different. In the insulating state we find the entropy to be around $1.8k_B$ per Mn site, while in the bad-metallic state it is increased to $2.3k_B$, which corresponds to 35 meV entropy gain across the transition, which is a decisive contribution to the free energy for the metal-insulator transition.

The important consequence of the Mott insulating t_{2g} states coexisting with the metallic e_g states at high temperature is the existence of the so-called *orbital-selective Mott state* (OSM), in which e_g electrons have enormous scattering rate (of the order of eV), and consequently small mobility so that there are no real bands present in the photoemission spectra, but rather just a very incoherent spectral weight (see Fig. 4). Photoemission on $LaMnO_3$ revealed that the system is of charge transfer type insulator, with strong admixture of oxygen p and Mn-e_g weight around 1 eV below the Fermi level [51,64]. In Ref. [65] a strong peak at approximately -3 eV and a shoulder between -1.5 eV and the Fermi level was identified, which we now interpret as the t_{2g} and e_g peak in the density of states, respectively. Even more revealing are optical experiments, which show a strongly temperature-dependent peak around 2 eV present only in the orbitally ordered state [66], and replaced by a broad distribution of optical weight above 800 K. By analyzing low-temperature data in Ref. [67] it was found that the 2 eV peak in optics comes from e_g-e_g transitions, and that t_{2g}-e_g transitions appear at 3.8 eV. This is all consistent with our spectra in Fig. 2(a), as the e_g-e_g distance is close to 2 eV and the t_{2g}-e_g distance is close to 4 eV at room temperature, while in disordered state above 800 K the gap disappears and the scattering rate broadens low-energy excitations. We note that in earlier DMFT works, the e_g-e_g splitting in the ordered state was somewhat too large ($\approx$3.5 eV [49] and $\approx$4 eV [50]), pointing again to the shortcomings of the low-energy Hubbard-type modeling. Finally we note that theoretical DOSs in Fig. 2 are plotted using experimental crystal structures, but the results do not change appreciably when the theoretical crystal structures are used.

While a large amount of experimental data is available for $LaMnO_3$, very little is known about $BiMnO_3$. Our calculations (Fig. 3) show a strong similarity with $LaMnO_3$, but also some important differences.

In particular, there is stronger anisotropy within the DOS of the t_{2g} and e_g orbitals for the Mn_2 ion compared to the Mn_1 ion [see Figs. 3(a) and 3(b)]. For example, there is a very sharp peak in the DOS of two t_{2g} orbitals at -2.0 eV and the e_g orbital at -0.6 eV, corresponding to the Mn_2 ion [Fig. 3(b)]. This is a consequence of the anisotropic hybridization between the lone-pair O-p and $Mn_2 - d$ orbitals. We recall that the lone pair of the Bi-6s state points toward the face of the distorted Mn_2O_6 octahedra as shown in

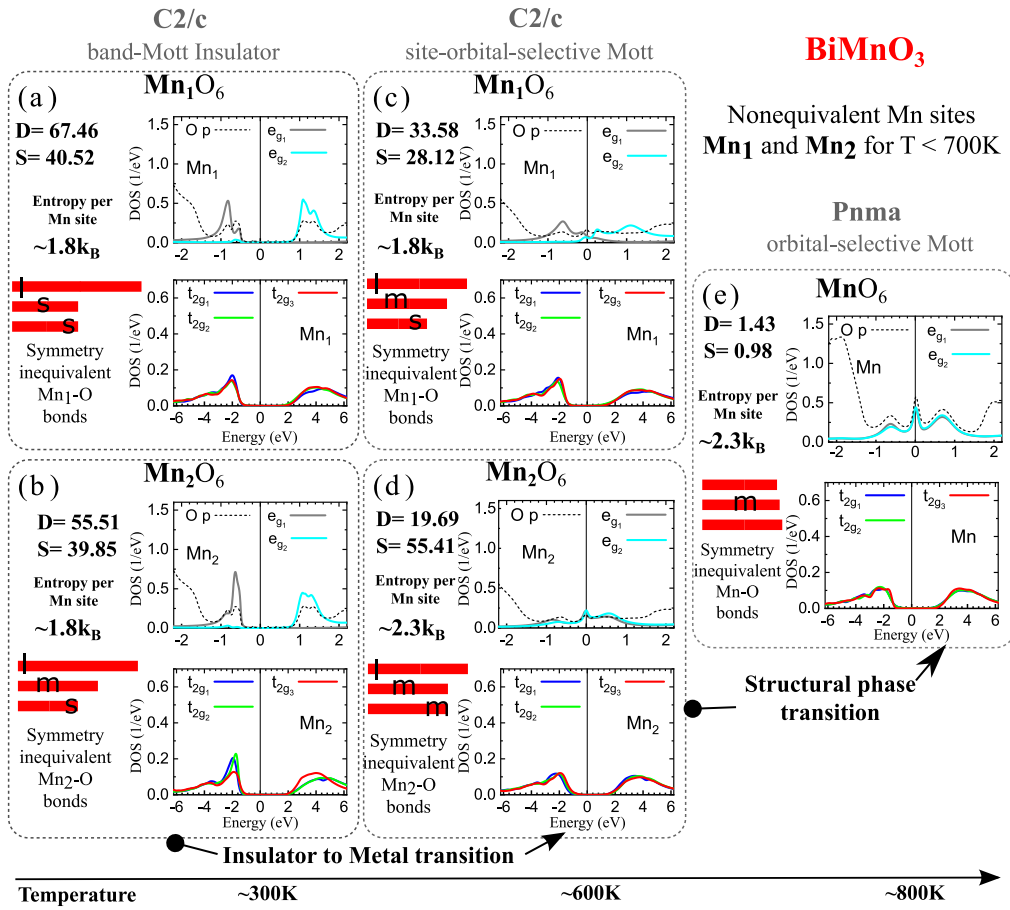

FIG. 3. Temperature-dependent electronic states in $BiMnO_3$. Panels (a) to (e) show for each inequivalent Mn octahedra the following properties: (1) values of the distortion indices, **D** and **S**; (2) electronic entropy per Mn site; (3) schematic view of the symmetry-inequivalent Mn-O bonds represented by red horizontal bars [the horizontal size of the bar is proportional to the bond length, short (s), medium (m), long (l); in panel (e) the three bonds are slightly distorted around the average bond length]; (4) e_g and t_{2g} projected density of states per formula unit versus energy in eV, for each electronic phase at a given temperature. On top of each panel we give the crystallographic symmetry at a given temperature and a name characterizing the electronic properties of the predicted electronic phases. The panels are connected by arrows suggesting the order parameter of the phase transitions.

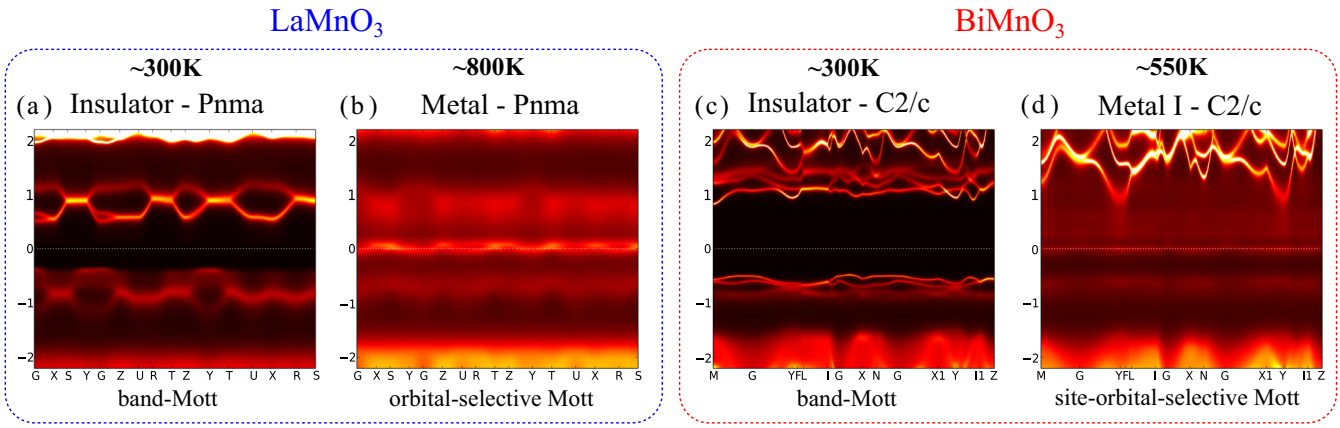

FIG. 4. Spectral functions for various novel phases in (Bi,La)MnO_3. For both compounds we give the spectral functions showing the metal-to-insulator phase transitions. In panels (a) and (b) we show the spectral functions for the band-Mott and orbital-selective Mott states for $LaMnO_3$; in panels (c) and (d) we show the spectral functions of the band-Mott and site-orbital-selective Mott states for $BiMnO_3$.

Fig. 1(d); thus this anisotropic hybridization is present in the system (see Ref. [68]). The anisotropic hybridization of the t_{2g} orbitals with the lone pair in the case of Mn_2 atoms is also confirmed by the fact that the Mn_1 atoms have similar distortions, but the corresponding DOS of the t_{2g} orbitals is isotropic [Fig. 3(a)]. The highly distorted monoclinic crystal structure of the $BiMnO_3$ compound is a consequence of the competition between the Jahn-Teller octahedra distortions that are squeezing the lone pair of the Bi-6*s* state. This is different from the case of the $LaMnO_3$ compound, where the lone pair is absent; thus the Jahn-Teller octahedra distortions appear in the orthorhombic crystal structure.

At room temperature, the local Jahn-Teller distortions for both inequivalent Mn ions are large enough to decrease the e_{g1} hybridization with the O-p states allowing localization of e_g electrons, even though the e_g orbitals also hybridize with the lone pair. These local distortions are depicted by red segments and given in terms of distortion indices in Figs. 3(a) and 3(b).

Note that larger values of the bond distortion index **D** in octahedra corresponds to more anisotropic hybridization between the two e_g orbitals and O-p states, causing orbital polarization and consequently localization of electrons. With increasing temperature our theoretical method reveals that the local Jahn-Teller distortions decrease (meaning smaller **D** values); thus the e_{g1} hybridization with the O-p states is increasing while the e_{g2} hybridization is decreasing (see Ref. [69]). At the same time the lone pair is exerting pressure on the neighboring ions to gain more space; thus it is contributing further to decreasing local distortions. Since the lone pair points toward the face of the Mn_2O_6 distorted octahedra, the local distortions of the Mn_2 site get reduced faster with increasing temperature than for the Mn_1 site. These local distortions are depicted by red segments and given in terms of distortion indices in Figs. 3(c) and 3(d). Consequently, when the local distortions are small enough, e_{g1} and e_{g2} hybridizations with the O-p states become similar; thus the e_g gap on Mn_2 ion collapses, and the system becomes bad metal. While decreasing the local distortions, the anisotropic hybridization of the t_{2g} with the lone-pair and O-p orbitals disappears; i.e., the resonance in the t_{2g} DOS disappears going from Figs. 3(b) to 3(d). However, the Mn_1 ion remains close to its low-temperature state, for one thing, its orbital occupancy in Table I remains unchanged, and the e_g states show DOS with a pseudogap [Fig. 3(c)]. Due to the qualitative difference in physical state on the two Mn ions, we call this state the *site-orbital-selective Mott* state, and we note that the orbital order remains strong only on the Mn_1 ion. Such partial orbital order on half of Mn ions is consistent with RXS experiments [43], in which the room temperature signal was roughly a factor of two stronger than in the intermediate state. Surprisingly, the entropy on Mn atoms is very weakly temperature dependent between the room temperature and the first transition (around 600 K), at which the entropy on Mn_2 increases for $0.5k_B$, while the entropy on Mn_1 remains almost unchanged. Only at the second transition around 800 K the entropy of Mn_1 increases to its saturated value within the bad metallic state.

We also note that the electronic spectral weight of the t_{2g} orbitals pointing toward the lone pair is strongly temperature dependent; therefore treating t_{2g} electrons as a fixed core spin would not result in correct prediction of the crystal structures.

Figure 4 displays the single-particle spectral functions $A(\mathbf{K}, \omega)$ in the insulating room temperature state, and in the first metallic state. The room temperature direct gaps in $LaMnO_3$ and $BiMnO_3$ are $\approx$0.8 eV and 1.2 eV, which are in decent agreement with optical experiments (0.9 eV in $LaMnO_3$ [66] and 1.2 eV in $BiMnO_3$ [70,71]). We note that the prediction of the gap size in $BiMnO_3$ seems to be very challenging for other *ab initio* methods, as the gap size is either too large (hybrid functional 1.7 eV [28]) or too small (modified Becke-Johnson exchange functional 0.75 eV [72]; 0.5 eV or less by various LDA + U calculations [73–76]). Finally, the orbital-selective Mott phase, in which the orbital order is melted away, is displayed in Fig. 4(b). The spectral function has no sharp bands, only the incoherent spectral weight; hence the charge mobility is very low. This state is also realized in the ferromagnetic Kondo model of Ref. [62]; therefore it might show giant magnetoresistance. Figure 4(d) shows the new phase site-orbital-selective Mott state, realized in the intermediate temperature range where Mn_1 shows orbital ordering and Mn_2 does not. This state is a superposition of a very incoherent orbital-selective Mott phase and the insulating phase, which shows somewhat more sharp bands above 1 eV.

Figure 5 shows the comparison between the theoretical and experimental temperature dependence of the distortion index **D**. In $LaMnO_3$ it changes only for 20% between the room temperature and 550 K, while it collapses abruptly around 800 K. We note an excellent agreement between the theoretical and experimental distortion index. In $BiMnO_3$ the two Mn sites show very different behavior: The changes on Mn_1 are comparable to $LaMnO_3$ (20%), while on Mn_2 ion the distortion is almost complete at 550 K (80%). In the high-temperature phase the distortion is small but finite. The reason for such markedly different behavior of the two sites is that the Mn_2 ion hybridizes with the Bi-6*s* lone pair, while Mn_1 does not (see Ref. [77]). Finally, we note that the measured and theoretical distortion indexes have similar trend, except that the disproportionation between Mn_1 and Mn_2 seems a bit weaker in experiment than in theory [78].

IV. CONCLUSIONS

In conclusion, using eDMFT methods we found novel electronic states in the Mn perovskite system, such as the site-orbital-selective Mott state, which hosts Mott insulating t_{2g} states, and a combination of semimetallic and metallic e_g states on two inequivalent Mn atoms. We showed that the isostructural transition in $BiMnO_3$ at 474 K should be characterized as the insulator-metal transition at which half of Mn atoms give up the orbital order, while the fully disordered state is reached only at the structural transition of 768 K. We showed that the electronic entropy plays the decisive role in the metal-insulator transition in both compounds. By self-consistent determination of both the correlated electronic state and the corresponding relaxed crystal structure we showed that the temperature evolution of phases in $LaMnO_3$ and $BiMnO_3$ can be properly explained from first principles, thus demonstrating the predictive power of the eDMFT method for

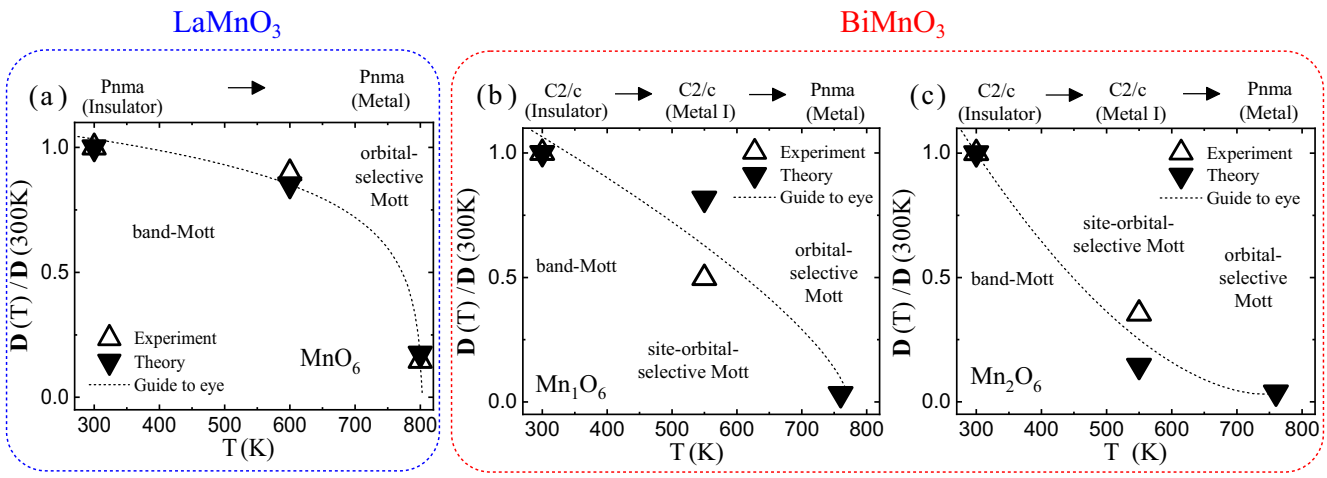

FIG. 5. Structural relaxations within LDA + eDMFT for all the temperature-dependent novel electronic phases in (Bi,La)MnO_3. In each panel we plot the bond distortion (**D**) index versus temperature, normalized to its values at room temperature. In panel (a) we plot **D** for the Mn site in $LaMnO_3$. In panels (b) and (c) we plot **D** for the two inequivalent Mn sites in $BiMnO_3$. Above each panel we give the temperature-dependent crystal symmetry and the properties of that electronic state (metal or insulator). The arrows point to the type of phase transition (structural or metal-insulator phase transition).

structural and electronic properties. In addition, we predict the temperature dependence of the spectral functions for the novel phases found in Mn perovskite systems, predictions that can be tested experimentally by ARPES.

ACKNOWLEDGMENTS

G.L.P. was supported by the U.S. Department of Energy, Office of Science, Basic Energy Sciences, as a part of the Computational Materials Science Program, funded by the U.S. Department of Energy, Office of Science, Basic Energy Sciences, Materials Sciences and Engineering Division, while at Rutgers and by a grant of the Romanian Ministry of Education and Research, CNCS-UEFISCDI, Project No. PN-III-P1-1.1-TE-2019-1767, within PNCDI III while at USV. K.H. was supported by the NSF, Grant No. DMR-1709229.

G.L.P. carried out the calculations. K.H. developed the code. G.L.P. and K.H. analyzed the results and wrote the paper.

The authors declare no competing interests.

[1] E. Dagotto, T. Hotta, and A. Moreo, Colossal magnetoresistant materials: The key role of phase separation, Phys. Rep. **344**, 1 (2001).

[2] A. P. Ramirez, Colossal magnetoresistance, J. Phys.: Condens. Matter **9**, 8171 (1997).

[3] M. Imada, A. Fujimori, and Y. Tokura, Metal-insulator transitions, Rev. Mod. Phys. **70**, 1039 (1998).

[4] D. Khomskii, Multiferroics: Different ways to combine magnetism and ferroelectricity, J. Magn. Magn. Mater. **306**, 1 (2006).

[5] Y. Tokura and N. Nagaosa, Orbital physics in transition-metal oxides, Science **288**, 462 (2000).

[6] DFT + embedded DMFT functional, http://hauleweb.rutgers.edu/tutorials, where for the DFT part we are using the WIEN2K code: P. Blaha, K. Schwarz, G. K. H. Madsen, D. Kvasnicka, J. Luitz, R. Laskowski, F. Tran, and L. D. Marks, *WIEN2K, An Augmented Plane Wave + Local Orbitals Program for Calculating Crystal Properties* (Karlheinz Schwarz, Technische Universität Wien, Austria, 2018).

[7] K. Haule, C.-H. Yee, and K. Kim, Dynamical mean-field theory within the full-potential methods: Electronic structure of $CeIrIn_5$, $CeCoIn_5$, and $CeRhIn_5$, Phys. Rev. B **81**, 195107 (2010).

[8] K. Haule, Structural predictions for correlated electron materials using the functional dynamical mean field theory approach, J. Phys. Soc. Jpn. **87**, 041005 (2018).

[9] J. H. Shim, K. Haule, and G. Kotliar, Fluctuating valence in a correlated solid and the anomalous properties of delta-plutonium, Nature (London) **446**, 513 (2007).

[10] M. Janoschek, P. Das, B. Chakrabarti, D. L. Abernathy, M. D. Lumsden, J. M. Lawrence, J. D. Thompson, G. H. Lander, J. N. Mitchell, S. Richmond, M. Ramos, F. Trouw, J.-X. Zhu, K. Haule, G. Kotliar, and E. D. Bauer, The valence-fluctuating ground state of plutonium, Sci. Adv. **1**, e1500188 (2015).

[11] S. Mandal, R. E. Cohen, and K. Haule, Strong pressure-dependent electron-phonon coupling in FeSe, Phys. Rev. B **89**, 220502(R) (2014).

[12] S. Gerber, S.-L. Yang, D. Zhu, H. Soifer, J. A. Sobota, S. Rebec, J. J. Lee, T. Jia, B. Moritz, C. Jia, A. Gauthier, Y. Li, D. Leuenberger, Y. Zhang, L. Chaix, W. Li, H. Jang, J.-S. Lee, M. Yi, G. L. Dakovski *et al.*, Femtosecond electron-phonon lock-in by photoemission and x-ray free-electron laser, Science **357**, 71 (2017).

[13] Z. P. Yin, K. Haule, and G. Kotliar, Kinetic frustration and the nature of the magnetic and paramagnetic states in iron pnictides and iron chalcogenides, Nat. Mater. **10**, 932 (2011).

[14] M. Liu, L. W. Harriger, H. Luo, M. Wang, R. A. Ewings, T. Guidi, H. Park, K. Haule, G. Kotliar, S. M. Hayden, and P. Dai, Nature of magnetic excitations in superconducting $BaFe_{1.9}Ni_{0.1}As_2$, Nat. Phys. **8**, 376 (2012).

[15] K. Ohta, R. E. Cohen, K. Hirose, K. Haule, K. Shimizu, and Y. Ohishi, Experimental and Theoretical Evidence for Pressure-Induced Metallization in FeO with Rocksalt-Type Structure, Phys. Rev. Lett. **108**, 026403 (2012).

[16] K. Haule and G. Kotliar, Arrested Kondo effect and hidden order in URu_2Si_2, Nat. Phys. **5**, 796 (2009).

[17] H.-H. Kung, R. E. Baumbach, E. D. Bauer, V. K. Thorsmølle, W.-L. Zhang, K. Haule, J. A. Mydosh, and G. Blumberg, Chirality density wave of the "hidden order" phase in URu_2Si_2, Science **347**, 1339 (2015).

[18] K. Haule and G. L. Pascut, Forces for structural optimizations in correlated materials within a DFT+embedded DMFT functional approach, Phys. Rev. B **94**, 195146 (2016).

[19] K. Haule and G. L. Pascut, Mott transition and magnetism in rare earth nickelates and its fingerprint on the x-ray scattering, Sci. Rep. **7**, 10375 (2017).

[20] T. N. Stanislavchuk, G. L. Pascut, A. P. Litvinchuk, Z. Liu, S. Choi, M. J. Gutmann, B. Gao, K. Haule, V. Kiryukhin, S.-W. Cheong, and A. A. Sirenko, Spectroscopic and first principle DFT+eDMFT study of complex structural, electronic, and vibrational properties of $M_2Mo_3O_8$ (m = Fe, Mn) polar magnets, Phys. Rev. B **102**, 115139 (2020).

[21] R. Seshadri and N. A. Hill, Visualizing the role of Bi 6s "lone pairs" in the off-center distortion in ferromagnetic $BiMnO_3$, Chem. Mater. **13**, 2892 (2001).

[22] K. Momma and F. Izumi, *VESTA 3* for three-dimensional visualization of crystal, volumetric and morphology data, J. Appl. Crystallogr. **44**, 1272 (2011).

[23] M. Baldini, V. V. Struzhkin, A. F. Goncharov, P. Postorino, and W. L. Mao, Persistence of Jahn-Teller Distortion up to the Insulator to Metal Transition in $LaMnO_3$, Phys. Rev. Lett. **106**, 066402 (2011).

[24] P. M. M. Thygesen, C. A. Young, E. O. R. Beake, F. D. Romero, L. D. Connor, T. E. Proffen, A. E. Phillips, M. G. Tucker, M. A. Hayward, D. A. Keen, and A. L. Goodwin, Local structure study of the orbital order/disorder transition in $LaMnO_3$, Phys. Rev. B **95**, 174107 (2017).

[25] C. C. Chou, C. L. Huang, S. Mukherjee, Q. Y. Chen, H. Sakurai, A. A. Belik, E. Takayama-Muromachi, and H. D. Yang, Multiple magnetic transitions in multiferroic $BiMnO_3$, Phys. Rev. B **80**, 184426 (2009).

[26] A. A. Belik and E. Takayama-Muromachi, Effects of doping on structural, physical, and chemical properties of multiferroic $BiMnO_3$ and $BiCrO_3$, Trans. Mater. Res. Soc. Jpn. **34**, 39 (2009).

[27] A. A. Belik, Polar and nonpolar phases of $BiMO_3$: A review, J. Solid State Chem. **195**, 32 (2012).

[28] O. Diéguez and J. Íñiguez, Epitaxial phases of $BiMnO_3$ from first principles, Phys. Rev. B **91**, 184113 (2015).

[29] T. Kimura, S. Kawamoto, I. Yamada, M. Azuma, M. Takano, and Y. Tokura, Magnetocapacitance effect in multiferroic $BiMnO_3$, Phys. Rev. B **67**, 180401(R) (2003).

[30] A. A. Belik, T. Kolodiazhnyi, K. Kosuda, and E. Takayama-Muromachi, Synthesis and properties of oxygen non-stoichiometric $BiMnO_3$, J. Mater. Chem. **19**, 1593 (2009).

[31] J. Rodríguez-Carvajal, M. Hennion, F. Moussa, A. H. Moudden, L. Pinsard, and A. Revcolevschi, Neutron-diffraction study of the Jahn-Teller transition in stoichiometric $LaMnO_3$, Phys. Rev. B **57**, R3189(R) (1998).

[32] J.-S. Zhou and J. B. Goodenough, Paramagnetic phase in single-crystal $LaMnO_3$, Phys. Rev. B **60**, R15002(R) (1999).

[33] J. A. Souza, J. J. Neumeier, R. K. Bollinger, B. McGuire, C. A. M. dos Santos, and H. Terashita, Magnetic susceptibility and electrical resistivity of $LaMnO_3$, $CaMnO_3$, and $La_{1-x}Sr_xMnO_3 (0.13 \leqslant x \leqslant 0.45)$ in the temperature range 300–900 K, Phys. Rev. B **76**, 024407 (2007).

[34] F. Ramirez, B. Cunha, W. Alves, R. Jardim, R. Muccillo, and J. Souza, Structural, electronic, and magnetic entropy contributions of the orbital order-disorder transition in $LaMnO_3$, Phase Transitions **84**, 284 (2011).

[35] P. Mandal, B. Bandyopadhyay, and B. Ghosh, Resistivity anomaly in the vicinity of a structural phase transition in $La_{1-x}Sr_xMnO_3$, Phys. Rev. B **64**, 180405(R) (2001).

[36] A. A. Belik, S. Iikubo, T. Yokosawa, K. Kodama, N. Igawa, S. Shamoto, M. Azuma, M. Takano, K. Kimoto, Y. Matsui, and E. Takayama-Muromachi, Origin of the monoclinic-to-monoclinic phase transition and evidence for the centrosymmetric crystal structure of $BiMnO_3$, J. Am. Chem. Soc. **129**, 971 (2007).

[37] T. Yokosawa, A. A. Belik, T. Asaka, K. Kimoto, E. Takayama-Muromachi, and Y. Matsui, Crystal symmetry of $BiMnO_3$: Electron diffraction study, Phys. Rev. B **77**, 024111 (2008).

[38] P. Toulemonde, P. Bordet, P. Bouvier, and J. Kreisel, Single-crystalline $BiMnO_3$ studied by temperature-dependent x-ray diffraction and Raman spectroscopy, Phys. Rev. B **89**, 224107 (2014).

[39] R. Krüger, B. Schulz, S. Naler, R. Rauer, D. Budelmann, J. Bäckström, K. H. Kim, S.-W. Cheong, V. Perebeinos, and M. Rübhausen, Orbital Ordering in $LaMnO_3$ Investigated by Resonance Raman Spectroscopy, Phys. Rev. Lett. **92**, 097203 (2004).

[40] I. V. Solovyev and Z. V. Pchelkina, Orbital ordering and magnetic interactions in $BiMnO_3$, New J. Phys. **10**, 073021 (2008).

[41] R. Colella and Q. Shen, Resonant scattering and multiple Bragg x-ray diffraction in $LaMnO_3$: A classical view, Acta Cryst. A: Found Cryst. **62**, 459 (2006).

[42] Y. Murakami, J. P. Hill, D. Gibbs, M. Blume, I. Koyama, M. Tanaka, H. Kawata, T. Arima, Y. Tokura, K. Hirota, and Y. Endoh, Resonant X-Ray Scattering from Orbital Ordering in $LaMnO_3$, Phys. Rev. Lett. **81**, 582 (1998).

[43] C.-H. Yang, J. Koo, C. Song, T. Y. Koo, K.-B. Lee, and Y. H. Jeong, Resonant x-ray scattering study on multiferroic $BiMnO_3$, Phys. Rev. B **73**, 224112 (2006).

[44] H. Sawada, Y. Morikawa, K. Terakura, and N. Hamada, Jahn-Teller distortion and magnetic structures in $LaMnO_3$, Phys. Rev. B **56**, 12154 (1997).

[45] T. Hashimoto, S. Ishibashi, and K. Terakura, Jahn-Teller distortion and magnetic structure in $LaMnO_3$: A first-principles theoretical study with full structure optimizations, Phys. Rev. B **82**, 045124 (2010).

[46] D. W. Boukhvalov and I. V. Solovyev, Defects of the crystal structure and Jahn-Teller distortion in $BiMnO_3$, Phys. Rev. B **82**, 245101 (2010).

[47] M. R. Ahmed and G. A. Gehring, Volume collapse in $LaMnO_3$ studied using an anisotropic Potts model, Phys. Rev. B **79**, 174106 (2009).

[48] Y. S. Glazkova, A. A. Belik, A. V. Sobolev, and I. A. Presniakov, Local crystal structure of multiferroic $BiMnO_3$ studied by ^{57}Fe probe Mössbauer spectroscopy, Inorg. Mater. **52**, 499 (2016).

[49] E. Pavarini and E. Koch, Origin of Jahn-Teller Distortion and Orbital Order in $LaMnO_3$, Phys. Rev. Lett. **104**, 086402 (2010).

[50] I. Leonov, D. Korotin, N. Binggeli, V. I. Anisimov, and D. Vollhardt, Computation of correlation-induced atomic displacements and structural transformations in paramagnetic $KCuF_3$ and $LaMnO_3$, Phys. Rev. B **81**, 075109 (2010).

[51] T. Saitoh, A. E. Bocquet, T. Mizokawa, H. Namatame, A. Fujimori, M. Abbate, Y. Takeda, and M. Takano, Electronic structure of $La_{1-x}Sr_xMnO_3$ studied by photoemission and x-ray-absorption spectroscopy, Phys. Rev. B **51**, 13942 (1995).

[52] K. Haule, Exact Double Counting in Combining the Dynamical Mean Field Theory and the Density Functional Theory, Phys. Rev. Lett. **115**, 196403 (2015).

[53] See Supplemental Materials B to E at [http://link.aps.org/supplemental/10.1103/PhysRevB.107.045147] for experimental and predicted crystal structures of $BiMnO_3$ and $LaMnO_3$ at various temperatures.

[54] See Supplemental Material A at [http://link.aps.org/supplemental/10.1103/PhysRevB.107.045147] for the predicted crystal structure of $BiMnO_3$ at high temperatures.

[55] See Supplemental Material F to H at [http://link.aps.org/supplemental/10.1103/PhysRevB.107.045147] for the self-energies of the correlated orbitals which gives information about the gap type.

[56] V. Anisimov, I. Nekrasov, and D. E. Kondakov, Orbital-selective Mott-insulator transition in $Ca_{2-x}Sr_xRuO_4$, Eur. Phys. J. B **25**, 191 (2002).

[57] L. de'Medici, A. Georges, and S. Biermann, Orbital-selective Mott transition in multiband systems: Slave-spin representation and dynamical mean-field theory, Phys. Rev. B **72**, 205124 (2005).

[58] A. Georges, L. d. Medici, and J. Mravlje, Strong correlations from Hunds coupling, Annu. Rev. Condens. Matter Phys. **4**, 137 (2013).

[59] C. Zener, Interaction between the d-shells in the transition metals. II. Ferromagnetic compounds of manganese with perovskite structure, Phys. Rev. **82**, 403 (1951).

[60] P. W. Anderson and H. Hasegawa, Considerations on double exchange, Phys. Rev. **100**, 675 (1955).

[61] P. G. de Gennes, Effects of double exchange in magnetic crystals, Phys. Rev. **118**, 141 (1960).

[62] N. Furukawa, Transport properties of the Kondo lattice model in the limit $S = \infty$ and $D = \infty$, J. Phys. Soc. Jpn. **63**, 3214 (1994).

[63] K. Haule and T. Birol, Free Energy from Stationary Implementation of the DFT + DMFT Functional, Phys. Rev. Lett. **115**, 256402 (2015).

[64] See Supplemental Material M at [http://link.aps.org/supplemental/10.1103/PhysRevB.107.045147] for a comparison of DOS with ultraviolet photoemission spectra for $LaMnO_3$.

[65] J.-H. Park, C. T. Chen, S.-W. Cheong, W. Bao, G. Meigs, V. Chakarian, and Y. U. Idzerda, Electronic Aspects of the Ferromagnetic Transition in Manganese Perovskites, Phys. Rev. Lett. **76**, 4215 (1996).

[66] K. Tobe, T. Kimura, Y. Okimoto, and Y. Tokura, Anisotropic optical spectra in a detwinned $LaMnO_3$ crystal, Phys. Rev. B **64**, 184421 (2001).

[67] N. N. Kovaleva, A. V. Boris, C. Bernhard, A. Kulakov, A. Pimenov, A. M. Balbashov, G. Khaliullin, and B. Keimer, Spin-Controlled Mott-Hubbard Bands in $LaMnO_3$ Probed by Optical Ellipsometry, Phys. Rev. Lett. **93**, 147204 (2004).

[68] See Supplemental Material I at [http://link.aps.org/supplemental/10.1103/PhysRevB.107.045147] for the hybridization of the correlated orbitals for the $BiMnO_3$ band-Mott state.

[69] See Supplemental Material J at [http://link.aps.org/supplemental/10.1103/PhysRevB.107.045147] for the temperature dependence of the hybridization of the correlated orbitals for the $BiMnO_3$.

[70] J. H. Lee, X. Ke, R. Misra, J. F. Ihlefeld, X. S. Xu, Z. G. Mei, T. Heeg, M. Roeckerath, J. Schubert, Z. K. Liu, J. L. Musfeldt, P. Schiffer, and D. G. Schlom, Adsorption-controlled growth of $BiMnO_3$ films by molecular-beam epitaxy, Appl. Phys. Lett. **96**, 262905 (2010).

[71] X. S. Xu, J. F. Ihlefeld, J. H. Lee, O. K. Ezekoye, E. Vlahos, R. Ramesh, V. Gopalan, X. Q. Pan, D. G. Schlom, and J. L. Musfeldt, Tunable band gap in $Bi(Fe_{1-x}Mn_x)O_3$ films, Appl. Phys. Lett. **96**, 192901 (2010).

[72] X. Zhu, X. Chen, and B. Liu, First principles investigation of electronic and magnetic structures of centrosymmetric $BiMnO_3$ using an improved approach, Solid State Commun. **243**, 65 (2016).

[73] Z.-G. Mei, S.-L. Shang, Y. Wang, and Z.-K. Liu, First-principles study of structural and elastic properties of monoclinic and orthorhombic $BiMnO_3$, J. Phys.: Condens. Matter **22**, 295404 (2010).

[74] J. A. McLeod, Z. V. Pchelkina, L. D. Finkelstein, E. Z. Kurmaev, R. G. Wilks, A. Moewes, I. V. Solovyev, A. A. Belik, and E. Takayama-Muromachi, Electronic structure of $BiMO_3$ multiferroics and related oxides, Phys. Rev. B **81**, 144103 (2010).

[75] L. Bi, A. R. Taussig, H.-S. Kim, L. Wang, G. F. Dionne, D. Bono, K. Persson, G. Ceder, and C. A. Ross, Structural, magnetic, and optical properties of $BiFeO_3$ and Bi_2 $FeMnO_6$ epitaxial thin films: An experimental and first-principles study, Phys. Rev. B **78**, 104106 (2008).

[76] T. Shishidou, N. Mikamo, Y. Uratani, F. Ishii, and T. Oguchi, First-principles study on the electronic structure of bismuth transition-metal oxides, J. Phys.: Condens. Matter **16**, S5677 (2004).

[77] See Supplemental Material K at [http://link.aps.org/supplemental/10.1103/PhysRevB.107.045147] for the hybridization of the Bi 6s lone pair with $Mn_2$$d$ states in $BiMnO_3$.

[78] See Supplemental Material L at [http://link.aps.org/supplemental/10.1103/PhysRevB.107.045147] for DOS calculations using the experimental and theoretical crystal structures in $BiMnO_3$.